Science Advances
AAAS

advances.sciencemag.org/cgi/content/full/6/14/eaaz4344/DC1

Supplementary Materials for

MAP6 is an intraluminal protein that induces neuronal microtubules to coil

Camille Cuveillier, Julie Delaroche, Maxime Seggio, Sylvie Gory-Fauré, Christophe Bosc, Eric Denarier, Maria Bacia, Guy Schoehn, Hervé Mohrbach, Igor Kulić, Annie Andrieux*, Isabelle Arnal*, Christian Delphin*

*Corresponding author. Email: annie.andrieux@univ-grenoble-alpes.fr (A.A.); isabelle.arnal@univ-grenoble-alpes.fr (I.A.); christian.delphin@univ-grenoble-alpes.fr (C.D.)

Published 1 April 2020, *Sci. Adv.* **6**, eaaz4344 (2020)
DOI: 10.1126/sciadv.aaz4344

The PDF file includes:

Other Supplementary Material for this manuscript includes the following:

(available at advances.sciencemag.org/cgi/content/full/6/14/eaaz4344/DC1)

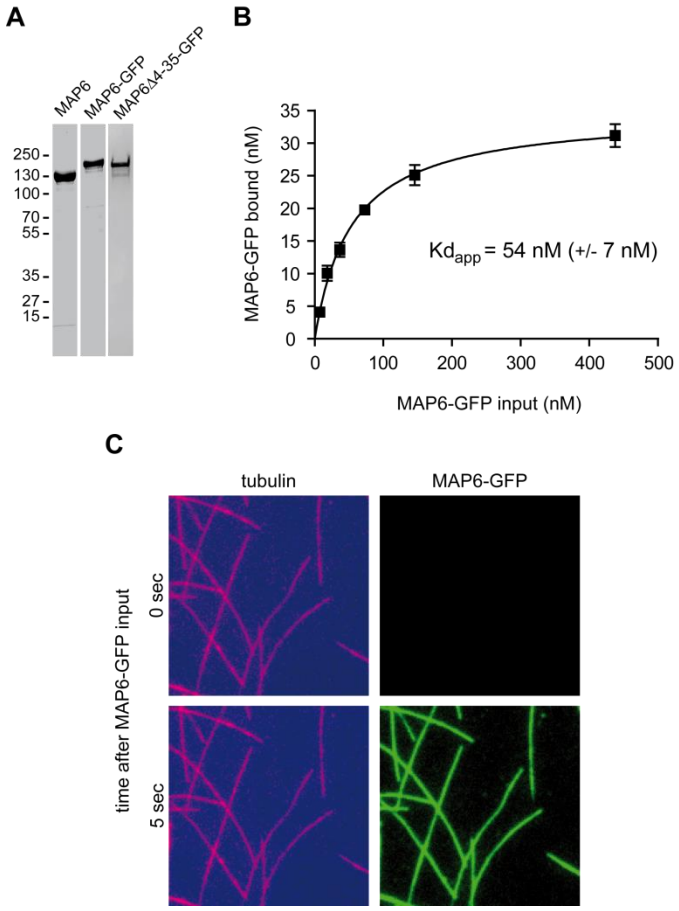

Fig. S1. Analysis of recombinant MAP6 proteins and binding with microtubules. (A) 1-2 µg of purified MAP6 recombinant proteins were analyzed by 10% SDS-polyacrylamide gel electrophoresis and Coomassie blue staining. Shown are the purified MAP6 protein, with and without a GFP tag, and a mutant form of the protein (discussed later in the text; see Fig. 3). **(B)** Increasing concentrations of MAP6-GFP were incubated with 200 nM of taxol-stabilized microtubules. After centrifugation, MAP6-GFP associated with microtubule and background levels were quantified with PHERAstar. We plotted the mean concentration of specific microtubule bound MAP6-GFP +/- SD, for at least three points in each condition, against the concentration of MAP6-GFP in the input. The binding curve and Kd value were obtained using a one-susbtrate-binding equation in GraphPad prism. (**C**) Microtubules observed by TIRF

microscopy before (top panels) and 5 sec after (bottom panels) addition of MAP6-GFP (150 nM) in the perfusion chamber.

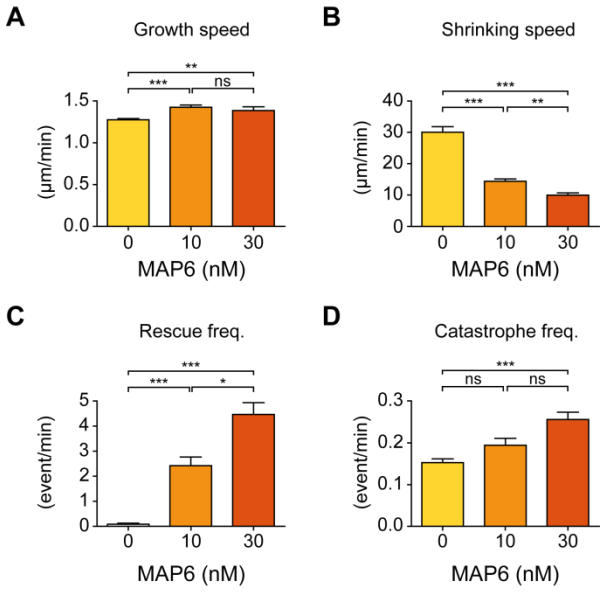

Fig. S2. Effects of MAP6 on microtubule dynamics. We extracted (A) growth rate, (B) shrinkage rate, (C) frequency of rescue events, and (D) frequency of catastrophe events from kymographs of microtubules polymerized in the presence of the indicated amounts of MAP6 (n = 44, 40, and 41 microtubules for conditions with 0, 10 and 30 nM of MAP6, respectively). * $p < 0.05$, ** $p < 0.01$, *** $p < 0.001$ (Kruskal-Wallis ANOVA followed by post-hoc Dunn's multiple comparison). ns: not significant.

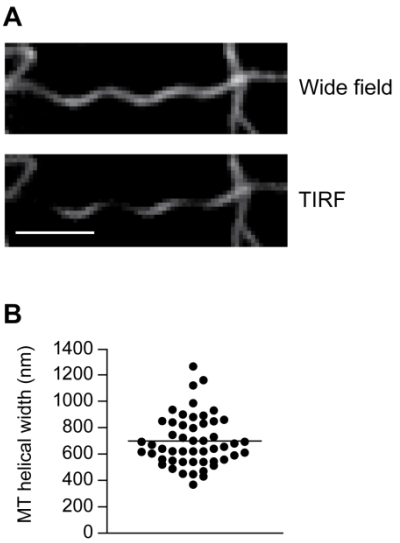

Fig. S3. Characterization of MAP6-induced microtubule structure. (A) A plain microtubule (wide field) grown in the presence of MAP6 appears as a dashed line in TIRF microscopy due to oscillation in the distance from the focal plane. Microtubules co-polymerized with 150 nM of MAP6 in TIRF conditions were washed to remove free tubulin, fixed with glutaraldehyde and imaged in TIRF or wide-field illumination. Scale bar, 5 µm. **(B)** Distribution of microtubule helical widths from microtubules polymerized in the presence of 200 nM of MAP6 and observed using airyscan microscopy. Mean: 0.70 µm +/- 0.19 (SD). n = 51 measures from 13 microtubules.

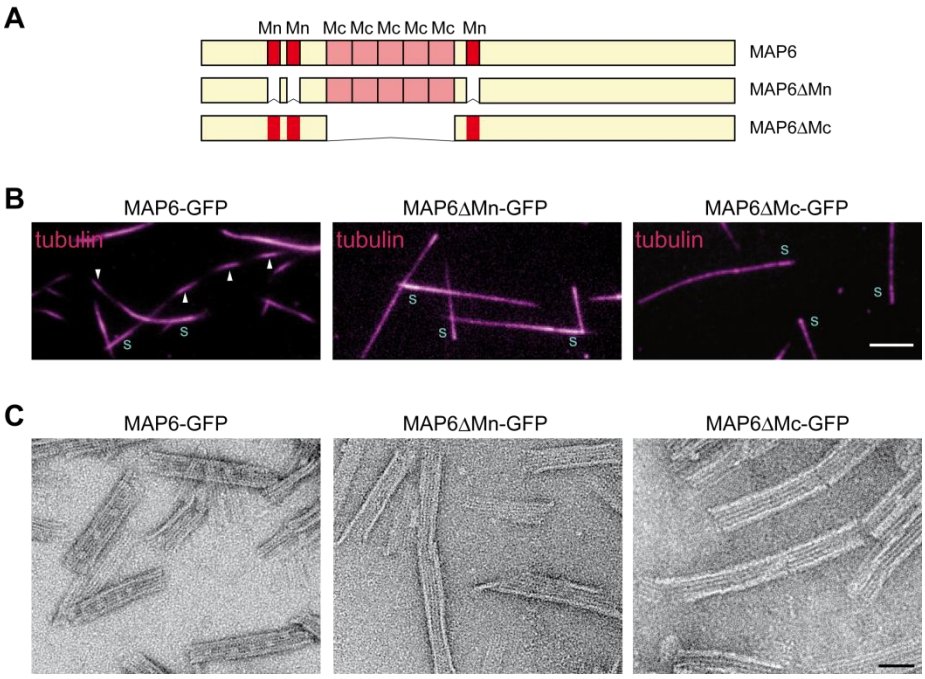

Fig. S4. MAP6 Mn and Mc domains are required for microtubule deformation and inner particles formation. (A) Scheme of MAP6 and MAP6ΔMn and MAP6ΔMc mutants, deleted for the temperature insensitive (Mn) or temperature sensitive (Mc) domains respectively. (B) TIRF images of microtubules grown for 90 min from GMPCPP seeds (s) in the presence of 200 nM of MAP6-GFP, MAP6ΔMn or MAP6ΔMc. Arrowheads point to the dashed appearance of microtubules. Scale bar, 5 µm. (C) Electron microscopy images of microtubules co-polymerized with MAP6-GFP, MAP6ΔMn or MAP6ΔMc in the presence of GMPCPP and processed for negative staining. Scale bar: 50 nm.

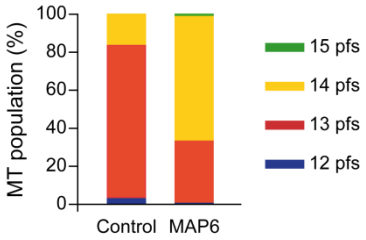

Fig. S5. MAP6 promotes the growth of 14-protofilament microtubules. Microtubules were polymerized in the absence of seeds from either 60 µM of tubulin (control) or 15 µM of tubulin in the presence of 300 nM of MAP6 and analyzed by cryo-electron microscopy (in the control, a higher concentration of tubulin is required for nucleation). Microtubule lattice organization was determined by the specific moiré fringe pattern resulting from the 2D projection of protofilaments (*32*). Proportions of microtubules with various numbers of protofilaments in the presence or absence of MAP6 are plotted as percentages of the total microtubule population. The total measured length of microtubules was 259 and 481 µm for control and MAP6 conditions, respectively.

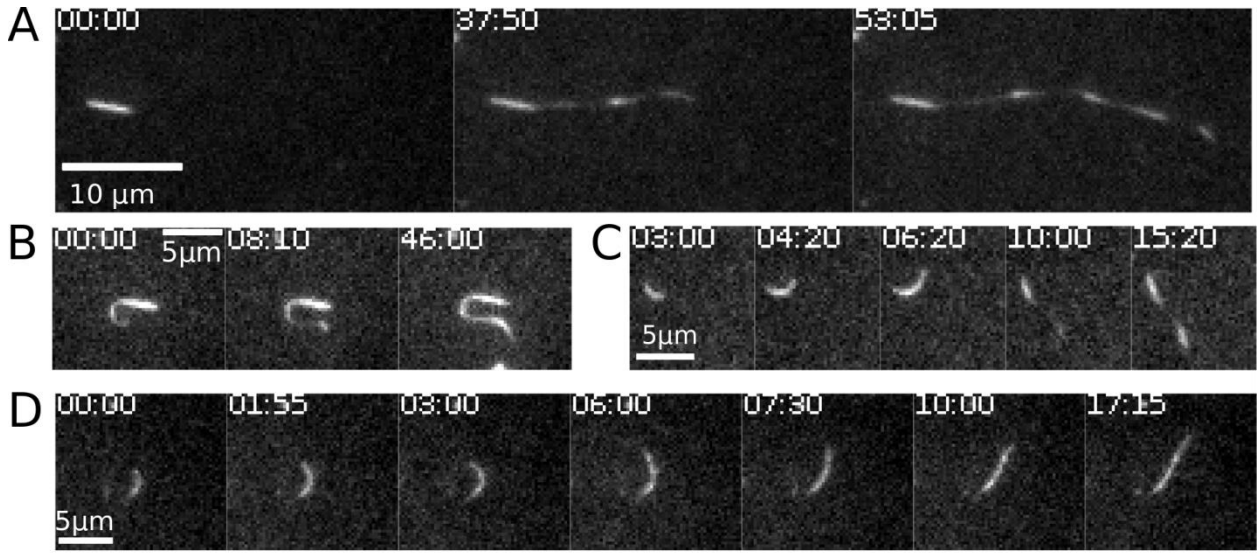

Fig. S6. Curvature of MAP6-stabilized microtubules. (A) Under TIRF time-lapse observation (time stamp min:sec), a large portion of microtubules displays a 5-7 µm pitched slender helix. (B) Occasionally, highly curved, stable arcs are observed at the growing end of microtubules. The arcs either persist in shape for long time intervals (B) or reshape (C, D) by leaving transiently the observation plane and finally switch to helical state as in (A).

Movie S1. Crop of a tomogram showing microtubules co-polymerized with MAP6 in the presence of GMPCPP.

Movie S2. Airyscan imaging of helical microtubules polymerized in the presence of MAP6. Microtubules were polymerized in a perfusion chamber from GMPCPP seeds in the presence of 10 µM of tubulin and 150 nM of MAP6 for 45 min. After removing free tubulin and fixation with glutaraldehyde by perfusion, microtubules were imaged with an airyscan microscope and analyzed using Zen 2.3 Desk software. Scale bars: 16.15 µm (red), 3.4 µm (green) and 1.36 µm (blue) in the x, y and z axes, respectively.

Movie S3. Straight helical growth of microtubule in the presence of MAP6. TIRF video microscopy of one growing microtubule. Speed: x500; Scale bar: 2 µm.

Supplementary Text

Model for microtubule curvature formation

The basic question that we intend to answer here is: how can an intact microtubule, which is a rigid tubular structure, transforms into a stable large-scale superhelix of micron-sized pitch and diameter? As previously suggested (*25, 26*), such a helix could be formed if a block of protofilaments shortens and bends outwards, while the tube is maintained. In the absence of internal twist, when the protofilaments are parallel, the tube will bend in the direction of the bent protofilament block and thus form an arc. When the protofilaments are twisted around the tube with a given internal pitch (which varies with the number of protofilaments) the microtubule adopts a helical shape.

What is the physical mechanism responsible for the outward bending of a block of protofilaments? As noted earlier (*25, 26*), the bending can be explained by a change of conformation at the level of the tubulin dimer that favors outward curving, propagates along a block of protofilaments and triggers the global bending of the microtubule as a minimum energy state.

There are two scenarios that might account for such an organization within the lattice:

(i) The tubulin dimers of the bent segment have switched to a different conformational state, with a block of protofilaments in a GDP state and the remaining ones in a GTP state. A perfectly organized separation between GDP or GTP-bound tubulins, which might result from the binding of MAPs or other molecules, appears very unlikely. But transient curved microtubule might form when the GTP hydrolysis is not homogeneous.

(ii) All tubulins in the lattice are in the GDP state but they are multistable entities that can fluctuate between a straight and a curved (shorter) conformation. With the additional condition of cooperativity, a conformational change in a block of protofilaments on one side of the microtubule lattice that occurs while the rest of the protofilaments stay unchanged would lead to lattice frustration and additional stress that can be reduced by a global microtubule bending and helical reshaping. In this case the helix results from the physical mechanism of spontaneous symmetry breaking.

We favor this second scenario, and present a model based on it below.

Multistability of tubulin

The two straight and curved/short switched states are compatible with our knowledge of the structure of the tubulin dimer. There seems to be a consensus that both GTP-tubulin and GDP-tubulin free dimers are curved in solution (*40*). The GTP-tubulin would be sufficiently

flexible to easily straighten during its incorporation into the lattice, which therefore stores little strain energy. This favors the polymerization of a stable microtubule. The change of the GDP-tubulin conformation from curved to straight, however, stores a larger strain energy in the lattice, resulting in a metastable microtubule subject to depolymerization (*41*). It has been observed that GDP-tubulin within the lattice polymerized with taxol can adopt an intermediate state between its straight and curved (free) state (*42*). Taxol is a small molecule that binds on the luminal face of β-tubulin and straightens the GDP-protofilaments, preventing GTP hydrolysis from putting strain on the lattice. Consistent with this observation, stable taxol-stabilized microtubules adopting a three-dimensional helicoid structure with a 15 μm pitch have been described (*43*). More recently, comparison of the GMPCPP (a stable analogue of GTP) and GDP reconstructions suggests a compaction at the dimer interface (called a "dimer rise" (*2*)) of the GDP tubulin with an axial dimer repeat reduction of 2.4% (*2*) instead of the intermediate curved conformation of the dimer itself (*42*). Lattice compaction is not observed when comparing the GMPCPP-taxol and GDP-taxol, in agreement with earlier studies (*44*); this effect is observed only during the co-polymerization of tubulin and taxol. If taxol is added after microtubule polymerization, there is global shortening (*44*). This implies that taxol is capable only of allosterically reversing the conformational switch of the dimer interface at the moment of GTP hydrolysis (*45*). We would therefore expect to observe a GTP-like straight (not compacted) microtubule instead of the helical microtubule observed in (*43*). It is not known whether taxol was added before or after polymerization in (*43*), but we suspect that helical conformations are observed only during co-polymerization.

There is no definite answer regarding the curved or compacted rise of GDP tubulins within the lattice. Since direct comparison of the GTP and GDP with taxol is not yet available, a slight curvature in the GDP form with respect to the GTP as observed in (*42*) might indeed exist.

In any case, as the model below shows, the assumption of conformational bistability between either straight/curved dimers, or extended/compacted tubulin rise and cooperativity, could account for a stable helical structure. There are some data that provide hints about bistability and cooperativity, at least for the curved case: observations of individual taxol-protofilaments show that straight and slightly curved protofilaments coexist at the same time, with a small preference for the curved state (*46*). This indicates that taxol-GDP tubulin is a metastable entity that can fluctuate between a straight and a curved state. The bimodal distribution of protofilaments implies that tubulin switching occurs simultaneously, suggesting a cooperative interaction along the protofilament (*46*). Based on the assumption of tubulin bistability and cooperativity, a model was built that proposes taxol-stabilized microtubules adopt a helical shape via a spontaneous symmetry-breaking mechanism (*25*). In the experiments of (*43*) an additional population with a larger curvature was observed over a longer period of time, suggesting some aging phenomenon. It was proposed that this large curvature can be activated by external forces and torques exerted by kinesin motors on gliding assays (*26*). An extension of the model (*25*) for microtubule gliding (*26*) led to the discovery of a mechanical hysteresis that quantitatively explains the formation of metastable curved microtubules moving in circles (*47*).

There are many other lines of evidence that binding molecules like motors, MAPs and drugs can change the lattice conformation by acting at the level of the tubulin. For instance, kinesin-1 binding shortens the dimer rise of the GMPCPP-microtubule by 0.8% but shows no effect on the compacted GDP-microtubule (*48*). On the other hand, the binding of KIF5C, a neuronal isoform of kinesin-1, on GDP-microtubule revealed an axial pitch elongation by 1.4% and a strong cooperativity of the tubulin dimers on the same protofilament (*49*). The KIF5C-induced extended GDP lattice also showed mechanical hysteresis, similar to gliding microtubules (*26*), as it kept its metastable elongated conformation for minutes after KIF5C dissociation (*49*).

In the experiment of reference (*49*), the GDP-microtubules are immobilized to the cover glass, rendering curvature in space impossible.

The experimental MAP6-microtubule co-polymerization conditions in the present study promote the growth of microtubules with 14 protofilaments that form large-scale superhelices of an average pitch of 5.5 µm and radius of 2.5 µm. This is a strong indication that the bending of the helix is triggered by a conformational change of tubulins in a block of protofilaments, the mechanism likely being similar to the one proposed for taxol-stabilized microtubules (*25*). . During co-polymerization, the microtubule grows as a stable superhelix and nanometer-sized luminal densities are observed. This shows that GTP hydrolysis, in addition to the presence of MAP6 in the lumen, is essential for the helical deformation. This suggests that MAP6 can multimerize and form an elastic network attached to the internal wall and that the densities are likely made of MAP6 multimers. The MAP6 tensile elastic network on the inner surface will thus counteract the compaction effect induced by GTP hydrolysis occurring on the exterior (*2, 44*). There is no direct proof of multimerization of MAP6 in the microtubule lumen, but only the MAP6 inside the microtubules forms particle densities, and the MAP6 bound to the outside is not visible by cryo-electron microscopy. This strongly suggests that there is a greater oligomeric fraction of MAP6 within the microtubule than outside it.

Basic Model Ingredients

We propose a frustrated core-shell model that is specific to the MAP6 sequence of binding, GTP hydrolysis, and microtubule bending involving the following four steps:

Step 1: Lumen binding. MAP6 co-polymerizes with tubulin and binds to the inner microtubule wall *before* hydrolysis (i.e., during co-polymerization),

Step 2: Multimerisation/Network formation. MAP6/MAP6 binding leads to formation

of a MAP6 elastic network within the lumen. As the diameter of the spherical lumen dots is ~ 9 nm, we can estimate a molecular mass of order ~ 400 kDa. As MAP6 has a mass ~ 100 kDa we can expect up to four MAP6 in a single particle density. Also there must be MAP6 regions for wall attachment (not clearly resolved so far, probably amorphous) and connectors between the particles. MAP6 multimerization combined with lumen binding gives rise to a definite elastic reference state of MAP6 with respect to the microtubule wall.

Step 3: GTP hydrolysis. Two scenarios are possible in this context for the change of conformation of the tubulin dimer: (i) the tubulin itself switches to a slightly curved state after GTP hydrolysis (*42*), or (ii) the hydrolysis of GTP leads to preferred compaction of the MAP6-tubulin dimer rise (*2*).

Step 4: Elastic shape instability). After hydrolysis followed by wall curving/shortening, there is now a mismatch between external and internal preferred elastic states. The wall prefers to be curved/shorter while the MAP6 elastic core in the lumen prefers to keep the straight/elongated state. This mismatch leads to microtubule-buckling and lattice curving.

This model is an adaptation of the previously proposed polymorphic lattice model (*26*), extended by the presence of an additional internal restoring spring force originating from the elastic MAP6 network. The presence of pre-stress in the model shares also some similarity with the surface-core instability model more recently developed for the curving instability of intermediate filaments (*50*). For vimentin filaments, the stress on the outside of the filament and its mismatch with the stress on the inside of it, lead to a conflict and a shape instability called autocoiling (*50*). The specificity of the current model for microtubules and MAP6 is that the tubulin dimer (or protofilaments) are already bistable by construction. In reference (*2*) the short state corresponds to a reduction $\varepsilon_0 = 2.4\%$ of the axial GDP tubulin dimer repeat. When an additional internal spring is added to restore the long state (the MAP6 network) and thus

counteracts the switching to the short state, we expect in general a smaller value of the reduction ε_0. Therefore, the MAP6-tubulin dimer complex is a single entity that can fluctuate between two conformations over an experimental time scale. The free energy difference between the two states must therefore be of the order of a few $k_B T$.

In summary, in this model the binding of MAP6 to the microtubule interior exerts a force that maintains extension whereas the exterior tends toward compaction. The facts and findings seem to agree and integrate well with the model. In particular the model explains the necessity for a) MAP6 + tubulin co-polymerization and b) GTP-GDP hydrolysis to occur in sequence in order for the microtubule to curve. If tubulin polymerizes first, *then* hydrolyses, *then* shortens and only *then* MAP6 is added, the latter stabilizes the lattice by binding (only) on the microtubule exterior. However, in this (reversed) scenario, it is the *curved/short* state of the lattice that is stabilized (as opposed to the long state stabilization in previous case). Thus, the steps of MAP6 binding and hydrolysis are not interchangeable and the necessary frustration is induced only upon co-polymerization followed by hydrolysis. Once the curvature is established, the conformation switching of GDP-tubulin to the *curved/short* state propagates along the protofilament axis. Naturally on this model, the helix follows the built-in protofilament pitch. This is the reason for the appearance of the helix instead of simple curved arcs.

Parameters of the Model

The polymorphic switchable model as presented here is general and thus adaptable to different situations as discussed in several papers (see for instance (*25*) and (*26*)). It requires only few parameters.

Known parameters.

They define the geometric and elastic properties of the MT. We have the number of

protofilaments N = 14, the inner and outer microtubule radii R_i = 7.5 nm and R_0 = 11.5 nm, the tubulin height $b \approx 8$ nm, which are known from crystallography (*51*). We need also the commonly used value of the bending stiffness of the microtubule $B = 10^{-23}$ Nm^2.

A priori unknown parameters

(i) The tubulin bistability assumption is associated with two physical quantities:

ΔG, the free energy difference between the long and short GDP-tubulin conformation which has to be of order of $k_B T$.

ε_0 , the tubulin strain. It is the relative length variation of the GDP-tubulin dimer when it switches from its long state to its short one.

(ii) The MAP6 are described as an elastic network attached to the interior wall of the MT and the stiffness of this network is given by the spring constant K. The sizes of the MAP6 particles do not explicitly enter the model

Outcome of the model

From the observed value of the radius of curvature R = 2.5 μm of the helical microtubules we obtained for a strain compaction of the basic unit $\varepsilon_0 \approx 0.6\%$ (see the mathematical details). In the absence of MAP6 or for small values of the MAP6 spring constant K, our model predicts that the helical state is only metastable. In this case, the ground state is a straight microtubule either long or short depending on the values of ΔG which favor either the long or short tubulin state. For large enough K and $\varepsilon_0 \approx 0.6\%$ the situation change drastically, as the ground state can be a superhelix with the characteristic experimentally observed. The road to this result can be followed from the details given in the next paragraph.

Mathematical details of the model

We consider a cross-section of a microtubule composed of N = 14 protofilaments. The total energy density is the sum of the elastic energies of the microtubule cross-section, the MAP6 network, and a switching energy:

$$e_{tot} = e_{el} + e_{switch}, \quad \text{(Eq. 1)}$$

where the transition energy e_{switch} comes from the hypothesis that every tubulin-MAP6 complex (indexed by n = 1...N = 14) has a free energy gain $\Delta G < 0$ to switch from the long state $\sigma = 0$ to the curved/short state $\sigma = 1$ (Fig. 5). Thus the transition energy density reads

$$e_{switch} = \frac{\Delta G}{b} \sum_{n=1}^{N} \sigma_n, \quad \text{(Eq 2)}$$

where b is either the tubulin height $b \approx 8$ nm in the case of tubulin curvature or the tubulin axial repeat (dimer rise) $b \approx 8.3$ nm in the case of interdimer interface compaction. The elastic energy density $e_{el} = e_{microtubule} + e_{MAP6}$ of the cross-section is the sum of the elastic energy of the lattice $e_{microtubule}$ and the elastic energy of the MAP6 network e_{MAP6}. We parameterize the microtubule cross-section by the azimuthal angle ϕ and the radial distance ρ to the centerline with $\rho \in [R_i, R_0]$ with R_i = 7.5 nm, R_0 = 11.5 nm the inner and outer microtubule radii, respectively, as known from crystallography (*51*). Denoted by Y the Young's modulus, we have

$$e_{microtubule} = \frac{Y}{2} \int_{R_i}^{R_0} \int_0^{2\pi} d\rho \rho d\phi (\varepsilon(r, \phi) - \varepsilon_{pref}(\rho, \phi))^2, \quad \text{(Eq. 3)}$$

where $\varepsilon(r, \phi) = -\vec{\kappa}\vec{\rho} + \bar{\varepsilon}$ is the inner strain with $\vec{\kappa} = (\kappa_x, \kappa_y)$ the centerline curvature vector, $\vec{\rho} = \rho(\sin\phi, \sin\phi)$ and $\bar{\varepsilon}$ the mean stretching strain of the cross section (*26*).

Each basic unit can also have a preferred strain ε_{pref} that can be either straight $\varepsilon_{pref}^{straight} = 0$ or switched $\varepsilon_{pref} = \varepsilon_{pref}^{switched}$. This is the bistability hypothesis. The preferred

switched strain on a tubulin $\varepsilon_{pref}^{switched}$ decomposes into two contributions $\varepsilon_{pref}^{switched} = \varepsilon_i$ for $\rho \in [R_i, R_m]$ and $\varepsilon_{pref}^{switched} = \varepsilon_0$ for $\rho \in [R_m, R_0]$. In the latter we will choose arbitrary to decompose the tubulin symmetrically with $R_m = \frac{R_i+R_0}{2} \simeq 10$ nm.

The elastic energy e_{MAP6} the MAP6 network can be written

$$e_{MAP6} = \frac{K}{2}(\bar{\varepsilon})^2, \qquad \text{(Eq.4)}$$

where *K* is the spring constant of the MAP6 network which has its lower energy in the extended state for $\bar{\epsilon} = 0$.

We consider a block of basic units of size *p* switched to the preferred state with $\varepsilon_{pref}^{switched}$, and $(N - p)$ of them remaining straight with $\varepsilon_{pref} = 0$. Choosing a particular direction for bending, for instance $\vec{\kappa} = (\kappa, 0)$, we have $\varepsilon(\rho, \phi) = -\kappa\rho\cos\phi + \bar{\varepsilon}$ and the total elastic energy after some short algebra becomes

$$\tilde{e}_{tot} = \frac{1}{2}\tilde{\kappa}^2 + \frac{1}{2}a_0\tilde{\varepsilon}^2 + \tilde{\kappa}\sin\frac{\phi_p}{2} + a_1\phi_p\bar{\varepsilon} + \gamma\phi_p + \frac{k}{2}(\bar{\varepsilon})^2 + const, \qquad \text{(Eq. 5)}$$

where $\phi_p = 2\pi\frac{p}{N}$ is the total azimuthal angle of the switched block. We have introduced the re-scaled total energy density $\tilde{e}_{tot} = \frac{e_{tot}}{(B\kappa_1^2)}$ and $\tilde{\kappa} = \frac{\kappa}{\kappa_1}$ the scaled curvature with the bending modulus defined as $B = Y\frac{\pi(R_0^4 - R_i^4)}{4}$ and the characteristic curvature

$$\kappa_1 = \frac{8}{3\pi}\frac{\varepsilon_i(R_m^3 - R_i^3) + \varepsilon_0(R_0^3 - R_m^3)}{R_0^4 - R_i^4} \qquad \text{(Eq. 6)}$$

which depends of the microtubule geometry and the preferred strains ε_i and ε_0. We have also introduced the rescaled dimensionless spring constant $k = \frac{K}{B\kappa_1^2}$ and the effective switching energy density

$$\gamma = a_2 + \frac{N\Delta G}{2\pi b B \kappa_1^2}\,. \qquad \text{(Eq. 7)}$$

In equations (5,7), we have introduced the dimensionless constants

$$a_0 = \frac{9\pi^2}{16}(R_0^2 - R_i^2)(R_0^4 - R_i^4)Q,$$

$$a_1 = \frac{9\pi}{32}(R_0^4 - R_i^4)(\varepsilon_i R_i^2 - \varepsilon_i R_m^2 + \varepsilon_0 R_m^2 - \varepsilon_0 R_0^2)Q,$$

$$a_2 = \frac{9\pi}{64}(R_i^4 - R_0^4)(\varepsilon_i^2(R_i^2 - R_m^2) + \left(\varepsilon_0^2(R_m^2 - R_0^2)\right)Q \qquad \text{(Eq. 8)}$$

with $Q = (\varepsilon_i R_i^3 - \varepsilon_i R_m^3 + \varepsilon_0 R_m^3 - \varepsilon_0 R_0^3)^{-2}$.

Minimizing the total energy with respect to $\bar{\varepsilon}$ and $\tilde{\kappa}$, i.e., solving $\frac{d}{d\bar{\varepsilon}}\tilde{e}_{tot} = 0 = \frac{d}{d\tilde{\kappa}}\tilde{e}_{tot}$, gives the optimal strain

$$\bar{\varepsilon}^{opt} = -\frac{a_1\phi_p}{a_0+k} \qquad \text{(Eq. 9)}$$

and the optimal curvature

$$\tilde{\kappa} = -\sin\frac{\phi_p}{2}. \qquad \text{(Eq. 10)}$$

Inserting these into (Eq. 5) yields the total energy density:

$$\tilde{e}_{tot}(\phi_p) = -\frac{c_p}{2}\phi_p^2 + \gamma\phi_p - \frac{1}{2}\sin^2\frac{\phi_p}{2} \qquad \text{(Eq. 11)}$$

where we omitted irrelevant terms without ϕ_p-dependence and introduced the dimensionless constants

$$c_p = \frac{a_1^2}{a_0+k}(1 - \frac{k}{a_0+k}) > 0. \qquad \text{(Eq. 12)}$$

Eq. (11) is our main result. It leads to a phase diagram with three phases: long, short and curved microtubules similar to (*26*). The long state corresponds to $\phi_p = 0$ for which $\bar{\varepsilon}^{opt} = 0$. The

maximum compaction is realized for $\phi_p = 2\pi$, yielding a short microtubule with $\bar{\varepsilon}^{opt} = -\frac{a_1 2\pi}{a_0+k}$. The curved microtubule is obtained for ϕ_p different for 0 and 2π. The regime of weak elastic force $k << a_0$, where $c_p = {a_1^2}/{a_0}$, was considered in (*26*) for microtubules in a gliding assay where a curved microtubule ground state was predicted for $c_p < 0.1$. In the limit of a very large elastic constant $k>>a_0$, we have $c_p \approx 0$, and Eq. (11) reduces to

$$\tilde{e}_{tot}(\phi_p) \approx \gamma\phi_p - \frac{1}{2}\sin^2\frac{\phi_p}{2} \qquad \text{(Eq.13)}$$

In this simplified case, $\bar{\varepsilon}^{opt} \approx 0$, as expected. The phase diagram that results from Eq. (13) depends only on the parameter γ given by Eq. (7) and was studied in (*25*) to explain how taxol induces a microtubule helix (*25, 43*) (where the lattice shortening strain ε was not taken into account). The result is that for $\gamma \lesssim -0.18$ the ground state is the short microtubule with $\phi_p = 2\pi$. For $\gamma \gtrsim 0.18$, the minimum energy is given by $\phi_p = 0$, corresponding to the long microtubule. Therefore, for $-0.18 \lesssim \gamma \lesssim 0.18$ the microtubule adopts a helical conformation for an angle ϕ_p different from 0 or 2π. We note that for $= 0$, the minimum is at $\phi_p = \pi$, i.e., half of the protofilaments are switched, displaying the state of maximal curvature. One can show that for a curved ground state, the number of basic elements *p* of a block that is switched lies in the range from 5 to 9.

Straight-curved tubulin state

In this first model, we consider a switched tubulin state that is curved, i.e.; $\varepsilon_{pref}^{switched} = \varepsilon_{pref}^{curved}$. This state can be obtained by assuming that MAP6 maintains the inner part of the basic unit straight, which means $\varepsilon_i = 0$. The outer part instead tends to shorten, i.e.; $\varepsilon_0 < 0$. In this case

$a_0 \approx \frac{14}{\varepsilon_0^2}$, $a_1 \approx -\frac{1.2}{\varepsilon_0}$ and $a_2 \approx 0.6$. The characteristic curvature (Eq. 6) becomes

$$\kappa_1 = \varepsilon_0 \frac{8}{3\pi} \frac{(R_0^3 - R_m^3)}{R_0^4 - R_i^4} \approx 40\varepsilon_0 \text{ µm}^{-1} \qquad \text{(Eq. 14)}$$

For $\varepsilon_0 \simeq -1\%$, one has $\kappa_1 \approx 0.4$ µm^{-1} and thus a radius of curvature $R_{(p)} = 1/(0.4\sin\left(\frac{\pi p}{14}\right))$ lying in the range 2.5 µm for $p = 7$ to 2.8 µm for $p = 5$ (or 9) in agreement with the observed average radius of curvature of the helical shape (Fig. 2D).

Remark: we have assumed that $R_m = \frac{R_i + R_0}{2} \approx 9.5$ nm. Another, less symmetrical choice is possible. For instance, $R_m = 10.5$ nm, thus closer to the outer side, leads to the same $\kappa_1 \approx 0.4$ µm^{-1} but for $\varepsilon_0 = -2\%$. In the absence of structural knowledge of the MAP6 tubulin complex, the value of ε_0 is arbitrary, although its range of magnitudes has to be very narrow, within a few percent. In the following we stay with $R_m \approx 9.5$ nm.

Can the observed superhelical microtubule with $R \sim 2.5$ µm be a ground state of the phase diagram resulting from Eq. (11)? For $\varepsilon_0 = -1\%$ we have $\alpha_0 \approx 1.4\ 10^5$ and $\alpha_1 \approx 120$. We expect that the existence of curved microtubule relies on the value of k, the spring constant of the MAP6 network acting on the inner size of the tubulin which opposes to the compaction of the outer side induced by GTP hydrolysis. Indeed, in the small restoring force regime $k << a_0$, we have $c_p \approx 0.1$ and the curved microtubule is not a ground state (but can be excited by external torque and force (*26*)). In this case the ground state is either short-straight or long-straight, depending on the value of γ.

On the other hand, in the opposite limit of $k >> a_0$, a curved state can become the ground state as far as $-0.18 \lesssim \gamma \lesssim 0.18$. Assuming the standard value $B = 10^{-23}$ Nm^2, the condition on γ leads to a switching free energy $|\Delta G| \approx 2k_BT$ which is a physically reasonable

number. The elastic MAP6 force per tubulin dimer $f = K|\bar{\varepsilon}^{opt}|/N$ takes a maximal value of $f \approx$ 40 pN. This value is reduced for smaller values of k. For instance for $k = 18{,}000$, the force $f \approx$ 5 pN is akin to the force exerted by a single kinesin on a tubulin. In this case $c_p \approx 0.08$ and the interval of the curved microtubule in the phase diagram is reduced to $\gamma \in [0.22, 0.28]$.

Extended-compacted tubulin state

In this second model, we assume that the tubulin dimers stay straight in the lattice but that dimer rise can be in an extended or compacted state. This situation can be modeled by assuming that $\varepsilon_i = \varepsilon_0 < 0$. In this case

$$\kappa_1 = \varepsilon_0 \frac{8}{3\pi} \frac{(R_0^3 - R_i^3)}{R_0^4 - R_i^4} \approx 65\varepsilon_0 \text{ µm}^{-1}. \quad \text{(Eq. 15)}$$

The same range of microtubule radius of curvature $R \in [2.5, 2.8]$ µm is obtained for a strain compaction of the basic unit $\varepsilon_0 \approx -0.6\%$. This shows that even a very small dimer rise compaction can lead to a strong microtubule deformation due to the cooperativity along the switched protofilaments. In this case $\alpha_0 \approx 1389$, $\alpha_1 \approx 13$ and $\alpha_2 \approx 0.4$. In the limit of large k we obtain a maximal value of the MAP6 elastic network force per tubulin of the order $f \approx 12$ pN. Smaller values can be reached for finite values of k. For instance, in the interval $\gamma \in [0.02, 0.23]$, we obtain this time $k \approx 950$ and a force $f \approx 5$ pN. We have a switching energy $|\Delta G| \approx$ 1.5 $k_B T$, similar to the previous case.

Dynamic microtubule curvature switching events

Our model presents a coherent interpretation of the origin of the stable superhelical microtubule conformation observed during the co-polymerization of tubulin and MAP6 (Fig.

S6A). Another remarkable phenomenon is the occasional observation of stable, highly curved arcs ($R\backsim$0.8 μm) at the growing microtubule end. The arcs either persist in shape for long time intervals while the end continues growing in a helical conformation (Fig. S6B) or they suddenly reshape by transiently leaving the observation plane and finally switch to helical states ($R \sim 2.5$ μm) (Fig S6C and S7D). The formation of highly curved arcs might correspond to scenario (i) presented at the beginning of the supplementary text. At an initial stage, by maintaining the tubulin dimer under tension, MAP6 might delay the hydrolysis of the GTP on one side of the microtubule cross-section, and the curvature builds up during the growth phase. This scenario can be understood with our model where now the lattice curvature can be seen as resulting from the bistability of tubulin between its GTP and GDP (with MAP6 binding) states with a strain ε_0 of the order -2% similar to (*2*). The slowed down, delayed hydrolysis can happen over long periods (seconds and minutes) and lead to a metastable lattice that can form a domain in contact with the helical state (Fig S6B). This metastable lattice could also switch quickly upon GTP hydrolysis to the helical state (with bistable GDP tubulins) as in Fig S6C and S6D. Therefore the cooperative curvature switching events, observed in early growth stage in the movies (with MAP6 + tubulin co-polymerized) are characteristic of the existence of various polymorphic states with different curvatures, as predicted by the model.

REFERENCES AND NOTES

1. P. W. Baas, A. N. Rao, A. J. Matamoros, L. Leo, Stability properties of neuronal microtubules. *Cytoskeleton* **73**, 442–460 (2016).

2. G. M. Alushin, G. C. Lander, E. H. Kellogg, R. Zhang, D. Baker, E. Nogales, High resolution microtubule structures reveal the structural transitions in αβ–tubulin upon GTP hydrolysis. *Cell* **157**, 1117–1129 (2014).

3. T. Mitchison, M. Kirschner, Dynamic instability of microtubule growth. *Nature* **312**, 237–242 (1984).

4. R. P. Tas, L. C. Kapitein, Exploring cytoskeletal diversity in neurons. *Science* **361**, 231–232 (2018).

5. C. Delphin, D. Bouvier, M. Seggio, E. Couriol, Y. Saoudi, E. Denarier, C. Bosc, O. Valiron, M. Bisbal, I. Arnal, A. Andrieux, MAP6-F is a temperature sensor that directly binds to and protects microtubules from cold-induced depolymerization. *J. Biol. Chem.* **287**, 35127–35138 (2012).

6. D. Job, C. T. Rauch, R. L. Margolis, High concentrations of STOP protein induce a microtubule super-stable state. *Biochem. Biophys. Res. Commun.* **148**, 429–434 (1987).

7. P. W. Baas, S. R. Heidemann, Microtubule reassembly from nucleating fragments during the regrowth of amputated neurites. *J. Cell Biol.* **103**, 917–927 (1986).

8. L. Guillaud, C. Bosc, A. Fourest-Lieuvin, E. Denarier, F. Pirollet, L. Lafanechère, D. Job, STOP proteins are responsible for the high degree of microtubule stabilization observed in neuronal cells. *J. Cell Biol.* **142**, 167–179 (1998).

9. A. Andrieux, P. A. Salin, M. Vernet, P. Kujala, J. Baratier, S. Gory-Faureé, C. Bosc, H. Pointu, D. Proietto, A. Schweitzer, E. Denarier, J. Klumperman, D. Job, The suppression of brain cold-stable microtubules in mice induces synaptic defects associated with neuroleptic-sensitive behavioral disorders. *Genes Dev.* **16**, 2350–2364 (2002).

10. J.-C. Deloulme, S. Gory-Fauré, F. Mauconduit, S. Chauvet, J. Jonckheere, B. Boulan, E. Mire, J. Xue, M. Jany, C. Maucler, A. A. Deparis, O. Montigon, A. Daoust, E. L. Barbier, C. Bosc, N. Deglon, J. Brocard, E. Denarier, I. Le Brun, K. Pernet-Gallay, I. Vilgrain, P. J. Robinson, H. Lahrech, F. Mann, A. Andrieux, Microtubule-associated protein 6 mediates neuronal connectivity through Semaphorin 3E-dependent signalling for axonal growth. *Nat. Commun.* **6**, 7246 (2015).

11. U. Gimenez, B. Boulan, F. Mauconduit, F. Taurel, M. Leclercq, E. Denarier, J. Brocard, S. Gory-Fauré, A. Andrieux, H. Lahrech, J. C. Deloulme, 3D imaging of the brain morphology

and connectivity defects in a model of psychiatric disorders: MAP6-KO mice. *Sci. Rep.* **7**, 10308 (2017).

12. A. Andrieux, P. Salin, A. Schweitzer, M. Bégou, B. Pachoud, P. Brun, S. Gory-Fauré, P. Kujala, M. F. Suaud-Chagny, G. Höfle, D. Job, Microtubule stabilizer ameliorates synaptic function and behavior in a mouse model for schizophrenia. *Biol. Psychiatry* **60**, 1224–1230 (2006).

13. A. Daoust, S. Bohic, Y. Saoudi, C. Debacker, S. Gory-Fauré, A. Andrieux, E. L. Barbier, J.-C. Deloulme, Neuronal transport defects of the MAP6 KO mouse—a model of schizophrenia—and alleviation by Epothilone D treatment, as observed using MEMRI. *Neuroimage* **96**, 133–142 (2014).

14. B. K. Garvalov, B. Zuber, C. Bouchet-Marquis, M. Kudryashev, M. Gruska, M. Beck, A. Leis, F. Frischknecht, F. Bradke, W. Baumeister, J. Dubochet, M. Cyrklaff, Luminal particles within cellular microtubules. *J. Cell Biol.* **174**, 759–765 (2006).

15. E. Nogales, M. Whittaker, R. A. Milligan, K. H. Downing, High-resolution model of the microtubule. *Cell* **96**, 79–88 (1999).

16. M. Ichikawa, K. H. Bui, Microtubule inner proteins: A meshwork of luminal proteins stabilizing the doublet microtubule. *Bioessays* **40**, 1700209 (2018).

17. M. K. Gardner, M. Zanic, C. Gell, V. Bormuth, J. Howard, Depolymerizing kinesins Kip3 and MCAK shape cellular microtubule architecture by differential control of catastrophe. *Cell* **147**, 1092–1103 (2011).

18. R. Mohan, E. A. Katrukha, H. Doodhi, I. Smal, E. Meijering, L. C. Kapitein, M. O. Steinmetz, A. Akhmanova, End-binding proteins sensitize microtubules to the action of microtubule-targeting agents. *Proc. Natl. Acad. Sci. U.S.A.* **110**, 8900–8905 (2013).

19. S. Guzik-Lendrum, I. Rayment, S. P. Gilbert, Homodimeric kinesin-2 KIF3CC promotes microtubule dynamics. *Biophys. J.* **113**, 1845–1857 (2017).

20. C. Bosc, R. Frank, E. Denarier, M. Ronjat, A. Schweitzer, J. Wehland, D. Job, Identification of novel bifunctional calmodulin-binding and microtubule-stabilizing motifs in STOP proteins. *J. Biol. Chem.* **276**, 30904–30913 (2001).

21. S. Gory-Fauré, V. Windscheid, C. Bosc, L. Peris, D. Proietto, R. Franck, E. Denarier, D. Job, A. Andrieux, STOP-like protein 21 is a novel member of the STOP family, revealing a Golgi localization of STOP proteins. *J. Biol. Chem.* **281**, 28387–28396 (2006).

22. L. Schaedel, K. John, J. Gaillard, M. V. Nachury, L. Blanchoin, M. Théry, Microtubules self-repair in response to mechanical stress. *Nat. Mater.* **14**, 1156–1163 (2015).

23. A. Vemu, E. Szczesna, E. A. Zehr, J. O. Spector, N. Grigorieff, A. M. Deaconescu, A. Roll-Mecak, Severing enzymes amplify microtubule arrays through lattice GTP-tubulin incorporation. *Science* **361**, eaau1504 (2018).

24. J. Atherton, M. Stouffer, F. Francis, C. A. Moores, Microtubule architecture in vitro and in cells revealed by cryo-electron tomography. *Acta Crystallogr. D Struct. Biol.* **74**, 572–584 (2018).

25. H. Mohrbach, A. Johner, I. M. Kulić, Cooperative lattice dynamics and anomalous fluctuations of microtubules. *Eur. Biophys. J.* **41**, 217–239 (2012).

26. F. Ziebert, H. Mohrbach, I. M. Kulić, Why microtubules run in circles: Mechanical hysteresis of the tubulin lattice. *Phys. Rev. Lett.* **114**, 148101 (2015).

27. S. Asakura, Polymerization of flagellin and polymorphism of flagella. *Adv. Biophys.* **1**, 99–155 (1970).

28. C. R. Calladine, Construction of bacterial flagella. *Nature* **255**, 121–124 (1975).

29. D. Chrétien, R. H. Wade, New data on the microtubule surface lattice. *Biol. Cell* **71**, 161–174 (1991).

30. S. Ray, E. Meyhöfer, R. A. Milligan, J. Howard, Kinesin follows the microtubule's protofilament axis. *J. Cell Biol.* **121**, 1083–1093 (1993).

31. A. A. Hyman, D. Chrétien, I. Arnal, R. H. Wade, Structural changes accompanying GTP hydrolysis in microtubules: Information from a slowly hydrolyzable analogue guanylyl-(alpha,beta)-methylene-diphosphonate. *J. Cell Biol.* **128**, 117–125 (1995).

32. R. H. Wade, D. Chrétien, Cryoelectron microscopy of microtubules. *J. Struct. Biol.* **110**, 1–27 (1993).

33. V. Soppina, J. F. Herbstman, G. Skiniotis, K. J. Verhey, Luminal localization of α-tubulin K40 acetylation by cryo-EM analysis of fab-labeled microtubules. *PLOS ONE* **7**, e48204 (2012).

34. C. Lazarus, M. Soheilypour, M. R. Mofrad, Torsional behavior of axonal microtubule bundles. *Biophys. J.* **109**, 231–239 (2015).

35. D. Dacheux, B. Roger, C. Bosc, N. Landrein, E. Roche, L. Chansel, T. Trian, A. Andrieux, A. Papaxanthos-Roche, R. Marthan, D. R. Robinson, M. Bonhivers, Human FAM154A (SAXO1) is a microtubule-stabilizing protein specific to cilia and related structures. *J. Cell Sci.* **128**, 1294–1307 (2015).

36. P. R. Burton, Luminal material in microtubules of frog olfactory axons: Structure and distribution. *J. Cell Biol.* **99**, 520–528 (1984).

37. A. Szyk, A. M. Deaconescu, J. Spector, B. Goodman, M. L. Valenstein, N. E. Ziolkowska, V. Kormendi, N. Grigorieff, A. Roll-Mecak, Molecular basis for age-dependent microtubule acetylation by tubulin acetyltransferase. *Cell* **157**, 1405–1415 (2014).

38. A. Hyman, D. Drechsel, D. Kellogg, S. Salser, K. Sawin, P. Steffen, L. Wordeman, T. Mitchison, Preparation of modified tubulins. *Methods Enzymol.* **196**, 478–485 (1991).

39. F. M. Coquelle, S. Blestel, C. Heichette, I. Arnal, C. Kervrann, D. Chrétien, Cryo-electron tomography of microtubules assembled in vitro from purified components. *Methods Mol. Biol.* **777**, 193–208 (2011).

40. A. Nawrotek, M. Knossow, B. Gigant, The determinants that govern microtubule assembly from the atomic structure of GTP-tubulin. *J. Mol. Biol.* **412**, 35–42 (2011).

41. M. Igaev, H. Grubmüller, Microtubule assembly governed by tubulin allosteric gain in flexibility and lattice induced fit. *eLife* **7**, e34353 (2018).

42. A. Krebs, K. N. Goldie, A. Hoenger, Structural rearrangements in tubulin following microtubule formation. *EMBO Rep.* **6**, 227–232 (2005).

43. P. Venier, A. C. Maggs, M.-F. Carlier, D. Pantaloni, Analysis of microtubule rigidity using hydrodynamic flow and thermal fluctuations. *J. Biol. Chem.* **269**, 13353–13360 (1994).

44. I. Arnal, R. H. Wade, How does taxol stabilize microtubules? *Curr. Biol.* **5**, 900–908 (1995).

45. E. H. Kellogg, N. M. A. Hejab, S. Howes, P. Northcote, J. H. Miller, J. F. Díaz, K. H. Downing, E. Nogales, Insights into the distinct mechanisms of action of taxane and non-taxane microtubule stabilizers from cryo-EM structures. *J. Mol. Biol.* **429**, 633–646 (2017).

46. C. Elie-Caille, F. Severin, J. Helenius, J. Howard, D. J. Muller, A. A. Hyman, Straight GDP-tubulin protofilaments form in the presence of taxol. *Curr. Biol.* **17**, 1765–1770 (2007).

47. L. A. Amos, W. B. Amos, The bending of sliding microtubules imaged by confocal light microscopy and negative stain electron microscopy. *J. Cell Sci. Suppl.* **14**, 95–101 (1991).

48. R. Zhang, B. LaFrance, E. Nogales, Separating the effects of nucleotide and EB binding on microtubule structure. *Proc. Natl. Acad. Sci. U.S.A.* **115**, E6191–E6200 (2018).

49. T. Shima, M. Morikawa, J. Kaneshiro, T. Kambara, S. Kamimura, T. Yagi, H. Iwamoto, S. Uemura, H. Shigematsu, M. Shirouzu, T. Ichimura, T. M. Watanabe, R. Nitta, Y. Okada, N. Hirokawa, Kinesin-binding–triggered conformation switching of microtubules contributes to polarized transport. *J. Cell Biol.* **217**, 4164–4183 (2018).

50. L. Bouzar, M. M. Müller, R. Messina, B. Nöding, S. Köster, H. Mohrbach, I. M. Kulić, Helical superstructure of intermediate filaments. *Phys. Rev. Lett.* **122**, 098101 (2019).

51. J. Howard, *Applied Mechanics Reviews* (Sinauer-Associates, 2001), vol. 55, chap. 3.